2025 18th International Congress on Image and Signal Processing, BioMedical Engineering and Informatics (CISP-BMEI) | 979-8-3315-7736-0/25/$31.00 ©2025 IEEE | DOI: 10.1109/CISP-BMEI68103.2025.11259211

Time dependent vector field reconstruction of moving macrophages- modeling, discretization, and results

Giulia Lupi [1*] , Karol Mikula [1*],

[1] Department of Mathematics, Slovak University of Technology, Radlinského 11, 81005 Bratislava, Slovakia

***Abstract*—In this paper, we suggest and study a new mathematical model for the reconstruction of time-dependent velocity vector fields. To that goal, we solve a minimization problem for two vector components and the vector length. Solving this problem leads to a system of partial differential equations with suitable boundary conditions. A special case of this general model, the reconstruction of a vector field from sparse samples by triple-Laplacian, was presented in [7], [8]. Here, we enhance the vector field reconstruction by additional smoothing and show its influence on the reconstruction results in time-dependent situations. The general form of the equations that we use for vector field reconstruction contain two terms: a diffusion term, which makes the vector field smoother, and an attracting term, which keeps the result close to the reconstruction from sparse samples. For the general model, we prove the existence and uniqueness of the weak solution. For the numerical solution, we use a finite difference method, where the unknowns are placed at the vertices of a pixel grid. We apply this mathematical model to reconstruct the time-dependent wound attractant field, which drives macrophages to the wound site during healing.**

***Index Terms*—Vector field reconstruction, Laplace operator, Sparse samples, Smoothing, Finite difference scheme, Macrophages**

I. Introduction

After an injury, danger signals released from the wound attract immune cells to the site of the wound, promoting tissue healing and eliminating potential pathogens. Biologists have extensively studied immune cell motion, analyzing differences between tissues and variations in the behavior of different cell types [1]–[3], [5], [13], [14]. Understanding immune cell movement as a whole is of significant clinical importance, as chronic inflammatory diseases and other pathologies are often linked to an excessive or unbalanced immune response. Identifying the key factors driving the motion of immune cells could help develop new strategies to prevent such dysregulated immune responses.

In this paper, we focus on a specific type of immune cell, macrophages, and study their behavior during wound healing. However, notice that the model presented in this paper offers a general approach for reconstructing time-varying vector fields in biomedical imaging. To apply the model to cell trajectories, the only assumption is that motion can be separated into random and directional parts, the directional part determined by a velocity vector field.

Various factors influence macrophage movement, including chemoattractants (which drive macrophage chemotaxis), inflammatory mediators, and changes in mechanical forces [9]. Throughout the paper, we refer to the velocity vector field that guides macrophages to the wound site as the *wound attractant field*. Reconstructing this field may provide biologists with insight into the mechanisms underlying macrophage motion. Furthermore, a time-dependent reconstruction can help answer key questions, such as how danger signals are released, their diffusion rate, and when their release ends.

The data sets analyzed were provided by the Laboratory of Pathogens and Host Immunity of the University of Montpellier. In all of them, zebrafish larvae were used to observe macrophage movement during wound healing. Three days after fertilization, the transgenic reporter larvae Tg (mfap4: mCherry-F) were used. These larvae express a farnesylated fluorescent protein, mCherry, under the control of the macrophage-specific mfap4 promoter, causing macrophages to show mCherry, i.e., red color, on their membranes. All larvae were wounded in the region of the tail fin fold and subsequently imaged throughout the healing process. A representative time frame of these videos is shown in Fig. 1. The

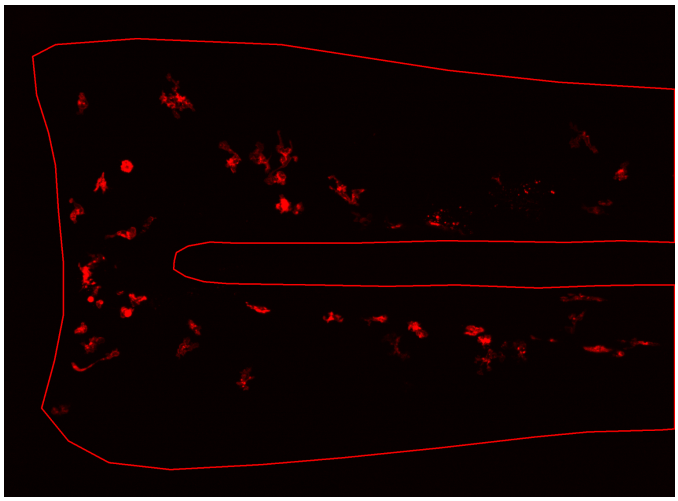

Fig. 1. Visualization of one frame of the 2D+time video of macrophages moving toward the wound. The transgenic reporter larvae used for the experiments express a fluorescent protein that allows us to see macrophages (in red color).

wound site is on the left side, and the macrophages, depicted

in red, are moving to the wound site, attracted by the wound attractant field. The continuous red lines show the boundary of the region where macrophages can move. The outer line is the fish border, while the inner one delimits the fish notochord, a region of the fish body in which macrophages cannot enter.

To address the problem of wound attractant field reconstruction, in [8] we developed a workflow to analyze macrophage motion during wound healing and reconstruct the wound attractant field using the information provided by macrophage trajectories. The tracking algorithm for 2D+time videos of macrophages moving towards a wound, developed in [11], allowed us to obtain trajectories of macrophages over time. Since macrophages show random and directional motion, we first smoothed the trajectories to separate the directional from random parts of the motion with the algorithm described in [6], [8]. The smoothing algorithm allowed us to find macrophage velocities on the smoothed trajectories. We then used these velocities as sparse samples for the reconstruction of the wound attractant field, cf. [8].

In this paper, we consider a more general mathematical model for vector field reconstruction that leads to the one described in [7], [8] for a specific choice of parameters and of the model domain. In particular, here, we first reconstruct the 2D time-dependent vector field from sparse samples and then apply additional smoothing. We consider the two domains Ω_r and Ω_s and the following minimization problem for the two vector components u_x and u_y and the vector length L

$$\min_u \frac{1}{2}\Big(\int_\Omega \|\nabla u\|^2 + \lambda \int_\Omega (u^0 - u)^2 \Big), \tag{1}$$

where $\Omega = \Omega_r$ or $\Omega = \Omega_s$, $\lambda \geq 0$ is a parameter, and u^0 is a function defined on Ω_s that will be defined in more detail in Section II. Solving the minimization problem (1) leads to solving the partial differential equation

$$-\Delta u = \lambda(u^0 - u) \tag{2}$$

with appropriate boundary conditions.

For $\lambda = 0$ and $\Omega = \Omega_r$, we obtain the model for vector field reconstruction from sparse samples in the form of triple-Laplacian

$$-\Delta u_i^r = 0, \quad i = 1, 2, 3. \tag{3}$$

where we consider $u_1 = u_x$, $u_2 = u_y$, and $u_3 = L$. In this case, we set Dirichlet boundary conditions for the sparse samples and zero Neumann boundary conditions for the model domain boundary. This model was described in [7], [8], where we proved the existence and uniqueness of a weak solution to the boundary value problem obtained by removing disjoint squares or a connected set of squares from the domain. In [7], [8], we considered the reconstruction of the stationary wound attractant field. Therefore, the macrophage velocities used as sparse samples were taken from every time step. In this paper, we consider the macrophage velocities in a given time interval and use them as sparse samples to reconstruct the time-dependent wound attractant field.

For the reconstruction of the vector field by additional smoothing, we set $\lambda > 0$ and $\Omega = \Omega_s$, and we obtain

$$-\Delta u_i^s = \lambda(u_i^0 - u_i^s), \ i = 1, 2, 3. \tag{4}$$

We set only zero Neumann boundary conditions on the model domain boundary. The smoothing equation comprises two terms: the diffusion term $-\Delta u$, which smooths the vector field, and the term $\lambda(u^0 - u)$ that keeps the solution close to u^0 depending on the value of λ. In our case, as will be explained in more detail in Section II, u^0 is a sufficiently smooth function on Ω_s equal to the reconstructed vector field on Ω_r obtained by solving (3). Here, $\lambda > 0$ is a parameter that controls the ratio of influence of the two terms in the equation. Therefore, it is clear that the smaller the λ, the smoother the solution of (4) will be.

In Section II, we will define the mathematical model for the vector field reconstruction first from sparse samples, see also [8], and then by additional smoothing. In both cases, the existence and uniqueness of a weak solution are proved. In Section III, we will write the numerical scheme for the general model presented in Section II. For the discretization of (3) and (4), we consider the finite-difference scheme with unknowns located on the vertices of the pixel grid given by the images of the 2D+time video. In Section IV, we will present results on real macrophage data.

II. Mathematical model

Thanks to the algorithm for smoothing of macrophage trajectories described in [8], we obtain the velocities on the smoothed trajectories. Each discrete point in the smoothed trajectories is then associated with a velocity vector and a time interval. We use these velocity vectors as sparse samples to reconstruct the velocity vector field that attracts macrophages to the site of the wound during wound healing. We will consider the 2 components of the vectors and the vector lengths separately; throughout the text, the term sparse sample will indicate the position and value of one of those. For the time-dependent vector field reconstruction, the sparse samples are considered in a given time interval. Equation (2) can be rewritten in the following more general form

$$-\Delta u + \lambda u = f, \tag{5}$$

where $\lambda \geq 0$ is a positive parameter and f is a sufficiently smooth function defined on the model domain Ω, where Ω will be either Ω_r or Ω_s. In particular, to prove the existence and uniqueness of a weak solution, Ω has to be a domain with a Lipschitz boundary and $f \in L^2(\Omega)$. Let us first define the model domains Ω_r for Eqs. (3) and Ω_s for Eqs. (4).

Consider $\tilde{\Omega}$ the auxiliary domain, that is, the image domain. In our application, the microscopy images the fish and the surrounding area, creating a one-time frame of the video. The fish is kept in the same position for the duration of the video. Since there is a part of the fish body where macrophages cannot move, experts draw approximate lines that mark the notochord and the boundary of the fish body. Therefore, we

first consider the cut domain Ω_s, an example of which is shown in Fig. 2 for one of the datasets. The outer rectangle represents the image domain $\tilde{\Omega}$, while the red area represents Ω_s. Let us

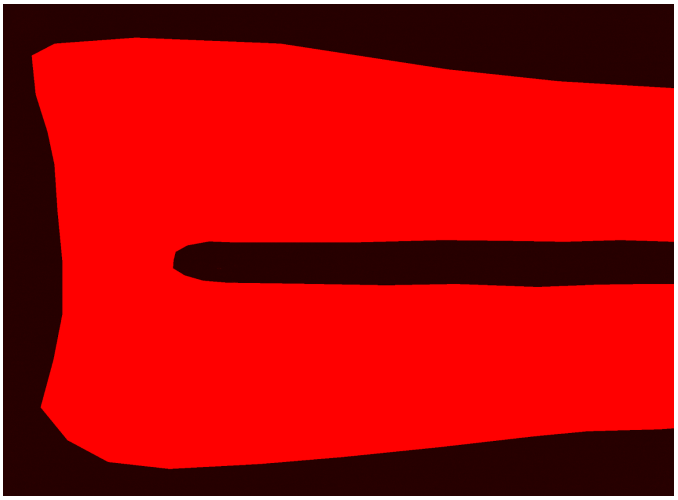

Fig. 2. Ω_s, region of the image domain where the wound attractant field is reconstructed.

define

$$\Gamma^2 = \partial\Omega_s \tag{6}$$

the domain boundary, cf. Fig. 1. Since Γ^2 is formed by contiguous edges of the image pixels, Ω_s is a domain with Lipschitz continuous boundary.

The idea for the definition of Dirichlet conditions inside Ω_s is to cut off the squares where the sparse samples are located. However, one must be careful doing so because the resulting cut domain Ω_r has to be a Lipschitz domain to be able to prove the existence and uniqueness of a weak solution. Since each discrete point of the macrophage trajectory is associated with a velocity vector, we consider a pixel grid of size $n_1 \times n_2$ and grid size h and check to which pixels the discrete points of the macrophage trajectories belong. Let us denote by S_p, $p = 1, ..., \tilde{s}$ the squares of size h where the sparse samples are located and by $v_p \in S_p$, $p = 1, ..., \tilde{s}$ the values in the center of the squares. To obtain a Lipschitz domain, it is necessary to impose some constraints on the squares S_p. First, we assume that the squares do not touch the model domain boundary Γ^2. Secondly, if two squares touch each other only in one vertex (creating a "bowtie-like" shape), we add another two squares and set their values as the mean value of the two squares having in common that vertex; see [8] for a more detailed description. If one of the two constraints is not satisfied, the resulting domain Ω_r will no longer be Lipschitz. Let us denote by S_p, $p = \tilde{s}+1, ..., s$ the added squares and by v_p, $p = \tilde{s}+1, ..., s$ the values in the centers of the added squares. Let us define

$$S = \bigcup_{p=1}^{s} \bar{S}_p \tag{7}$$

and

$$\Gamma^1 = \partial S. \tag{8}$$

Indicate by

$$\Omega_r = \Omega_s / S, \tag{9}$$

so that

$$\partial\Omega_r = \Gamma^2 \cup \Gamma^1. \tag{10}$$

As a final step, we need to define the continuous function g on the boundary Γ^1. Therefore, we need to define the values $u_{i,j} \in \partial S_p$ on the vertices of the squares. To do that, we consider the squares S_p of which $u_{i,j}$ is the value of one of the vertices; to each of such S_p, a value v_p is associated. Therefore, we set $u_{i,j}$ as the mean of those values v_p. The continuous function

$$g : \Gamma_1 \to \mathbb{R}, \tag{11}$$

is then defined in the following way. If two vertices $u_{i,j}$ of an edge of the square have the same value, then the value of g is set as constant on the edge. If the values of the vertices $u_{i,j}$ differ, then we define g on the edge as linearly changing from one value to the other.

Once we have defined the model domains Ω_r and Ω_s, we consider the boundary value problem

$$\begin{cases} -\Delta u^r(x) = 0, & x \in \Omega_r, \\ \frac{\partial u^r}{\partial \nu}(x) = 0, & x \in \Gamma^2, \\ u^r(x) = g(x), & x \in \Gamma^1, \end{cases} \tag{12}$$

for the vector field reconstruction from sparse samples and the boundary value problem

$$\begin{cases} -\Delta u^s(x) + \lambda u^s = \lambda u^0, & x \in \Omega_s, \\ \frac{\partial u^s}{\partial \nu}(x) = 0, & x \in \Gamma^2, \end{cases} \tag{13}$$

for the additional vector field smoothing. Here, $\lambda > 0$ and u^0 is defined as the solution of (12) in Ω_r and as the unique bilinear interpolation of the values $u_{i,j} \in \partial S_p$ in S_p. The proof of the existence and uniqueness of a weak solution of (12) and (13) can be done similarly to [7], [8]. We constructed the Lipschitz domains Ω_r and Ω_s; therefore, we can apply the theory of [10], [12].

Namely, let us consider the Lipschitz domain Ω and the general form (5). Notice that for $\lambda = 0$ and $\Omega = \Omega_r$ we obtain (12), therefore, the proof of the existence of a unique weak solution is done as in [8]. On the other hand, for $\lambda > 0$, $f = \lambda u^0$, and $\Omega = \Omega_s$, we can apply the theory of [10], [12] to the boundary value problem (13). In fact, the function

$$f = \lambda u^0 \in L^2(\Omega_s),$$

because $u^0 \in W_2^1(\Omega_r)$ and u^0 is bilinear in the finite number of squares S_p, $p = 1, ..., s$. Moreover, the bilinear form

$$A(v, w) = \sum_{l=1}^{2} \int_{\Omega_s} \frac{\partial v}{\partial l} \frac{\partial w}{\partial l} \, dx + \lambda \int_{\Omega_s} vw \, dx$$

is bounded and V-elliptic in $W_2^1(\Omega_s)$ for all $v, w \in W_2^1(\Omega_s)$. Indeed, since $\lambda > 0$, from the Schwartz and Hölder's inequalities it follows that $\forall v, w \in W_2^1(\Omega_s)$

$$\begin{aligned} |A(v, w)| &= \left| \int_{\Omega_s} \nabla v \cdot \nabla w \, dx + \lambda \int_{\Omega_s} vw \, dx \right| \leq \\ &\leq (\lambda + 1) \|v\|_{W_2^1(\Omega_s)} \|w\|_{W_2^1(\Omega_s)}, \end{aligned} \tag{14}$$

i.e. A is bounded. Moreover, $\forall v \in W_2^1(\Omega_s)$

$$|A(v,v)| = \left| \int_{\Omega_s} |\nabla v|^2 \, dx + \lambda \int_{\Omega_s} v^2 \, dx \right| \geq \\ \geq \min(1,\lambda) \|v\|^2_{W_2^1(\Omega_s)}, \tag{15}$$

i.e. A is V-elliptic. Therefore, since Ω_s is Lipschitz, we can apply Theorem 33.2 in [12] and prove the existence and uniqueness of a weak solution $u^s \in W_2^1(\Omega_s)$. Notice that the uniqueness of the solution in this case is given by the term λu^s with $\lambda > 0$. In Section III, we will show the finite difference scheme for discretization of (5), considering the boundary conditions on Γ^1 and Γ^2.

III. Numerical discretization

Let us consider the general form (5) of the PDE. Consider a square (pixel) grid of size $n_1 \times n_2$. For the finite-difference scheme, we consider the unknowns on the vertices of the pixels.

Initially, we create a mask M with size $(n_1+1)\times(n_2+1)$, where $n_1 \times n_2$ is the size of the image. We consider the values $v_{out}, v_{nbc}, v_{dbc}, v_{in} \in \mathbb{R}$ and set the mask values as follows.

- If the grid point (i,j) is in $\tilde{\Omega}/\bar{\Omega}_s$

$$M_{i,j} = v_{out}.$$

- If the grid point (i,j) is on Γ^2

$$M_{i,j} = v_{nbc}.$$

- If the grid point (i,j) is on Γ^1

$$M_{i,j} = v_{dbc}.$$

- If the grid point (i,j) is in Ω_r

$$M_{i,j} = v_{in}.$$

Also, if a grid point (i,j) on the boundary Γ^2 is such that $M_{i,j+1},\ M_{i,j-1},\ M_{i+1,j},\ M_{i-1,j} \neq v_{out}$, then we set $M_{i,j} = v_{in}$. In Fig. 3, is visualized the mask M for one of the data sets. In this case, the mask values were chosen as follows: $v_{dbc} = 100$, $v_{nbc} = 0$, $v_{out} = 200$, and $v_{in} = 255$ and represent the colors in Fig. 3. Notice that, when we consider the boundary value problem (13), we set $\Gamma^1 = \emptyset$ and $M_{i,j} = v_{in}$ for all $(i,j) \in \Omega_s$ so that we have only zero Neumann boundary conditions on the boundary Γ^2 of Ω_s. For the discretization of zero Neumann boundary conditions on Γ^2, we distinguish the various cases of the grid points. The grid point (i,j) on Γ^2 satisfies one of these conditions.

1) $M_{i,j+1},\ M_{i,j-1},\ M_{i-1,j} \neq v_{out}$ and $M_{i+1,j} = v_{out}$ or $i = n_1$, $j \in \{1,...,n_2-1\}$
2) $M_{i,j+1},\ M_{i,j-1},\ M_{i+1,j} \neq v_{out}$ and $M_{i-1,j} = v_{out}$ or $i = 0$, $j \in \{1,...,n_2-1\}$
3) $M_{i+1,j},\ M_{i,j-1},\ M_{i-1,j} \neq v_{out}$ and $M_{i,j+1} = v_{out}$ or $i \in \{1,...,n_1-1\}$, $j = n_2$
4) $M_{i+1,j},\ M_{i,j+1},\ M_{i-1,j} \neq v_{out}$ and $M_{i,j-1} = v_{out}$ or $i \in \{1,...,n_1-1\}$, $j = 0$

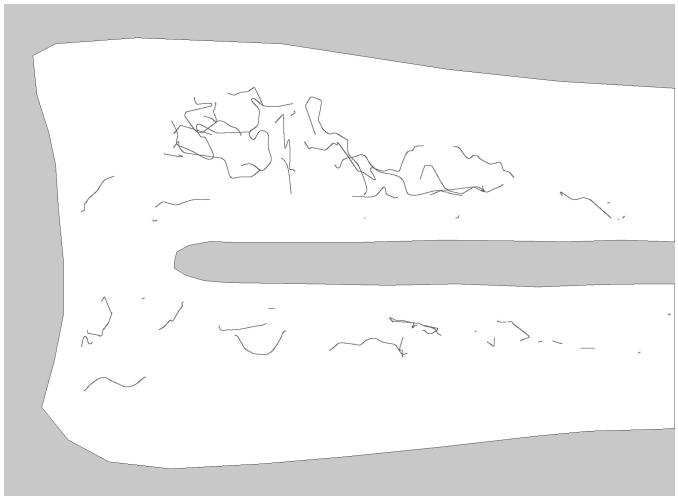

Fig. 3. Visualization of the mask $M_{i,j}$ for one of the datasets. In white is indicated Ω_r, in light grey the outside of the model domain, in black the boundary of Ω_s, and in dark grey the grid points where the Dirichlet conditions are prescribed.

5) $M_{i,j-1},\ M_{i-1,j} \neq v_{out}$ and $M_{i,j+1} = M_{i+1,j} = v_{out}$ or $i = n_1$, $M_{i,j+1} = v_{out}$ or $j = n_2$, $M_{i+1,j} = v_{out}$ or $i = n_1$, $j = n_2$
6) $M_{i,j-1},\ M_{i+1,j} \neq v_{out}$ and $M_{i,j+1} = M_{i-1,j} = v_{out}$ or $i = 0$, $M_{i,j+1} = v_{out}$ or $j = n_2$, $M_{i-1,j} = v_{out}$ or $i = 0$, $j = n_2$
7) $M_{i,j+1},\ M_{i+1,j} \neq v_{out}$ and $M_{i,j-1} = M_{i-1,j} = v_{out}$ or $i = 0$, $M_{i,j-1} = v_{out}$ or $j = 0$, $M_{i-1,j} = v_{out}$ or $i = 0$, $j = 0$
8) $M_{i,j+1},\ M_{i-1,j} \neq v_{out}$ and $M_{i,j-1} = M_{i+1,j} = v_{out}$ or $i = n_1$, $M_{i,j-1} = v_{out}$ or $j = 0$, $M_{i+1,j} = v_{out}$ or $i = n_1$, $j = 0$

Fig. 4 shows an example of a domain where zero Neumann boundary conditions are satisfied. In particular, we focus on condition 6, and the points where this condition is satisfied are marked as black circles. Let us indicate by $u_{i,j}$ the values of the function u, by $g_{i,j}$ the values of the Dirichlet conditions, and by $f_{i,j}$ the values of the function f in the grid points (i,j), $i = 0,...,n_1$, $j = 0,...,n_2$. We present in detail the following finite difference scheme, which is complex due to the general shape of the computational domains Ω_s and Ω_r and due to the fact that derivatives on the boundary Γ^2 are approximated in a second-order accurate way using mirroring of the solution values from the interior and boundary of the model domain.

- If $M_{i,j} = v_{in}$:

$$-u_{i,j+1} - u_{i,j-1} + (4+\lambda)u_{i,j} - u_{i-1,j} - u_{i+1,j} = f_{i,j}.$$

- If $M_{i,j} = v_{dbc}$:

$$u_{i,j} = g_{i,j}.$$

- If $M_{i,j} = v_{nbc}$:

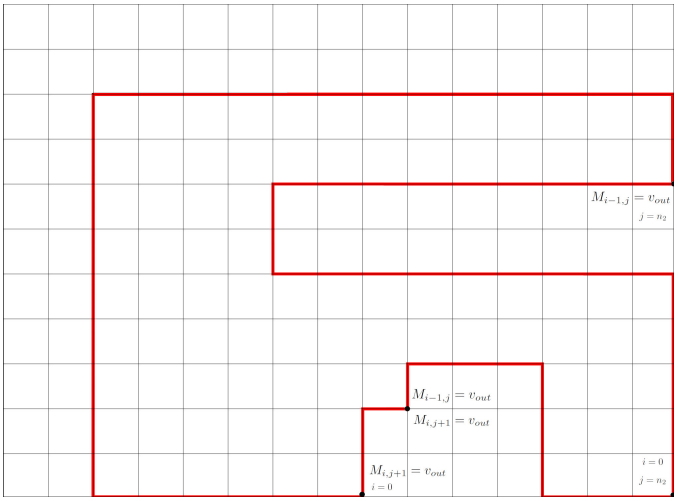

Fig. 4. Visualization of points (i, j) satisfying condition 6). The red line represents the boundary Γ^2 while the black circles represent the grid points where the condition is satisfied.

– If condition 1) is satisfied:

$$-u_{i,j+1} - u_{i,j-1} + (4+\lambda)u_{i,j} - 2u_{i-1,j} = f_{i,j}.$$

– If condition 2) is satisfied:

$$-u_{i,j+1} - u_{i,j-1} + (4+\lambda)u_{i,j} - 2u_{i+1,j} = f_{i,j}.$$

– If condition 3) is satisfied:

$$-2u_{i,j-1} + (4+\lambda)u_{i,j} - u_{i-1,j} - u_{i+1,j} = f_{i,j}.$$

– If condition 4) is satisfied:

$$-2u_{i,j+1} + (4+\lambda)u_{i,j} - u_{i-1,j} - u_{i+1,j} = f_{i,j}.$$

– If condition 5) is satisfied:

$$-2u_{i,j-1} + (4+\lambda)u_{i,j} - 2u_{i-1,j} = f_{i,j}.$$

– If condition 6) is satisfied:

$$-2u_{i,j-1} + (4+\lambda)u_{i,j} - 2u_{i+1,j} = f_{i,j}.$$

– If condition 7) is satisfied:

$$-2u_{i,j+1} + (4+\lambda)u_{i,j} - 2u_{i+1,j} = f_{i,j}.$$

– If condition 8) is satisfied:

$$-2u_{i,j+1} + (4+\lambda)u_{i,j} - 2u_{i-1,j} = f_{i,j}.$$

The system of equations is represented by a diagonally dominant matrix and, as such, can be solved directly. We used the SparseLU class from the Eigen library [4], which computes the LU decomposition of the sparse matrix representing the system and solves it efficiently and accurately.

IV. Results

We considered 2 different datasets; migrating macrophages were imaged 30 minutes after amputation, over 6 hours, with a time interval of 2.5 minutes between frames and a z-step of 1 µm. For all datasets, the pixel size was 0.319489 µm.

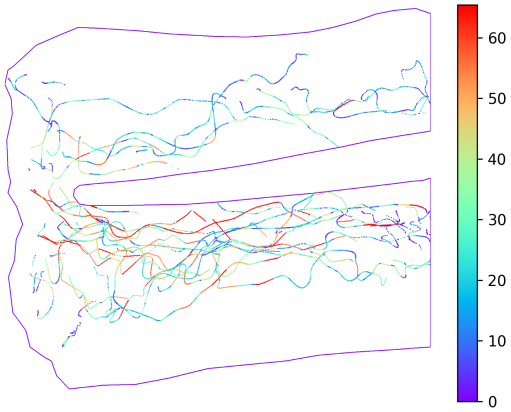

(a)

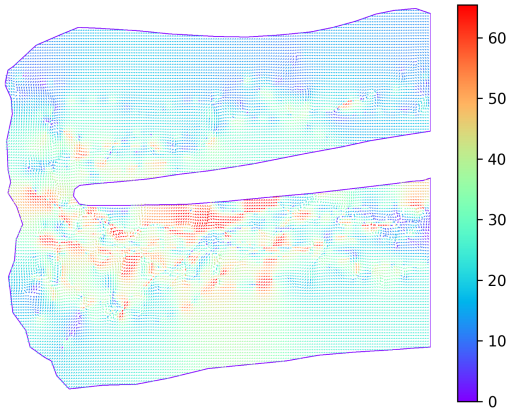

(b)

Fig. 5. 5(a): Visualization of the velocities on the smoothed trajectories. The color indicates the norm of the vectors. These velocities are used as sparse samples to reconstruct the wound attractant field driving the macrophages during wound healing. 5(b): Velocity vector field reconstructed solving the boundary value problem (12) with Dirichlet conditions for the sparse samples shown in Fig. 5(a).

For numerical experiments, we used 2D+time projection images, where the three-dimensional (3D) microscopy data were flattened into a 2D plane by applying a maximum intensity projection. In this method, the maximum intensity value along the z-axis was selected for each pixel.
In Fig. 5(a) are visualized the sparse samples extracted during the first 6 hours for one of the datasets; the color represents the norm of the vectors. In Fig. 5(b) we present the reconstructed

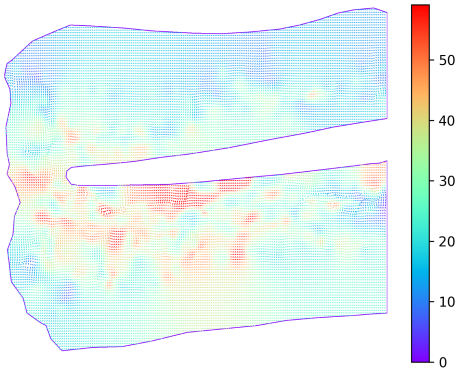

(a)

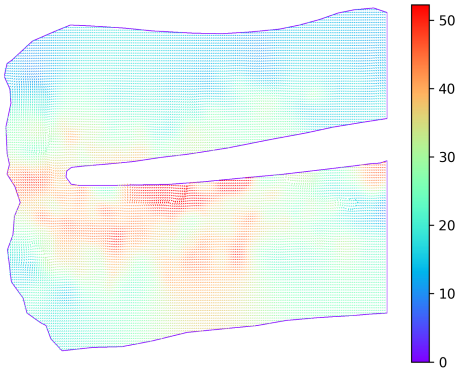

(b)

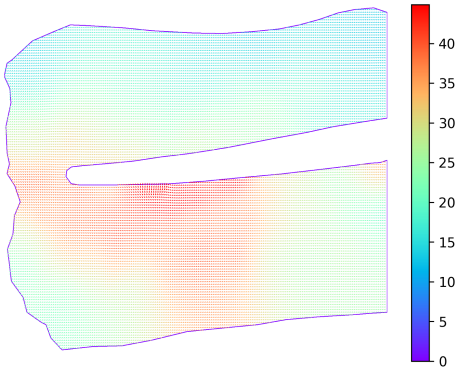

(c)

Fig. 6. Velocity vector field from Fig. 5(b) smoothed by solving the boundary value problem (13). 6(a): result of smoothing for $\lambda = 0.01$. 6(b): result of smoothing for $\lambda = 0.001$. 6(c): result of smoothing for $\lambda = 0.0001$.

wound attractant vector field considering the boundary value problem (12) with all sparse samples, cf. [8]. As one can see, the information given by the sparse samples, i.e., the direction and the speed (length of vectors), is extrapolated from the sparse samples where the vectors do not influence each other and are interpolated where the vectors influence each other.

Then, we considered smoothing of the reconstructed vector field, solving the boundary value problem (13). As stated above, the value of the parameter λ gives the ratio of influence between the smoothing term $-\Delta u$ and the term that keeps the solution close to u^0. Therefore, the smaller λ, the smoother the resulting vector field will be. We considered different values of λ and smoothed the reconstructed vector field from Fig. 5(b). Namely, we chose $\lambda = 0.01$, $\lambda = 0.001$, and $\lambda = 0.0001$; the results are shown in Fig. 6. Notice that if we choose a smaller value of λ, not only is the vector field smoother, but also the number of vectors directed toward the wound increases.

In the next numerical experiment, we present the reconstruction of the time-dependent vector field for the 2 datasets every hour, that is, from 1 to 6 hours. The reconstructed time-dependent vector field is obtained considering trajectories, i.e., sparse samples, only in a given time interval. The vector field is first reconstructed by solving the boundary value problem (12) and then smoothed by solving the boundary value problem (13) with $\lambda = 0.001$. From the time-dependent reconstruction, one might find information on the behavior of the wound attractant field over time; see Figs. 7, 8. In particular, in Figs. 7(a), 8(a), we considered the first hour of imaging, in Figs. 7(b), 8(b) the third and in Figs. 7(c), 8(c) the fifth hour of imaging. As one can notice, in the first and the fifth hours, the reconstructed vector fields show fast and directional motion towards the wound, while in the third hour, there is a decrease in both the speed and the directionality of the vector field. Notice that in Fig. 8(b), the fast motion is in the direction opposite to the wound.

In Fig. 9, we plotted the averaged velocity in x direction during the time for the 2 datasets. Notice that we chose the positive direction of the x axis as the direction of the wound. The values of the average velocity $\bar{v}_x$ of the 2 datasets are shown in blue for the data set in Fig. 7 and red for the data set in Fig. 8. The data sets show similar behavior: indeed, the average velocity $\bar{v}_x$ in the x direction is high in the first hour and gradually decreases for the second and third hours. Then, on the fourth and fifth hours, there is a second increase in the velocity toward the wound.

V. Conclusions

In this paper, we proposed a model for time-dependent vector field reconstruction. To define the mathematical model, we considered a minimization problem that leads to solving a partial differential equation for the two vector components and the vector lengths with appropriate boundary conditions. In particular, we set zero Neumann boundary conditions on part of the domain boundary and Dirichlet conditions on the complementary part of the domain boundary. Once we obtained the reconstruction of the vector field from sparse samples,

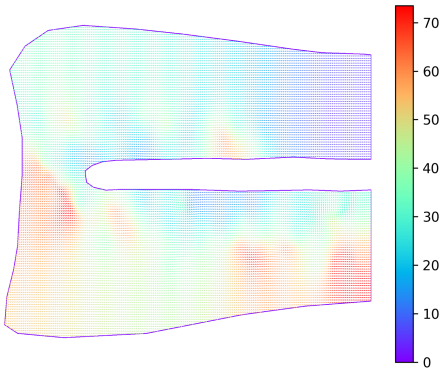

(a)

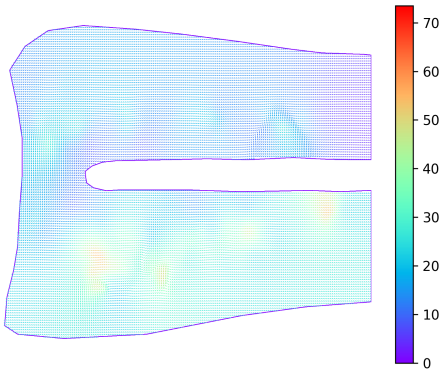

(b)

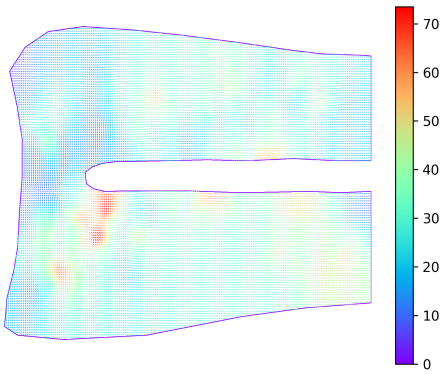

(c)

Fig. 7. Time dependent velocity vector field reconstruction. 7(a): result of reconstruction for the first hour. 7(b): result of reconstruction for the third hour. 7(c): result of reconstruction for the fifth hour.

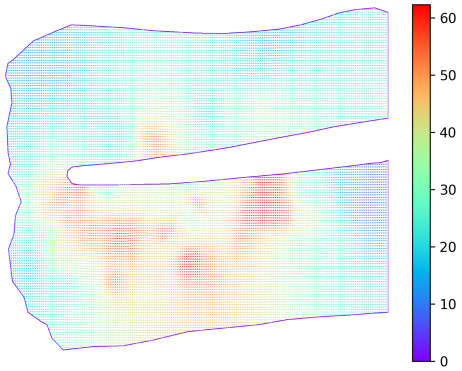

(a)

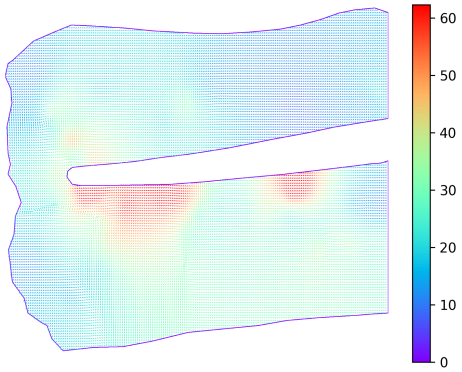

(b)

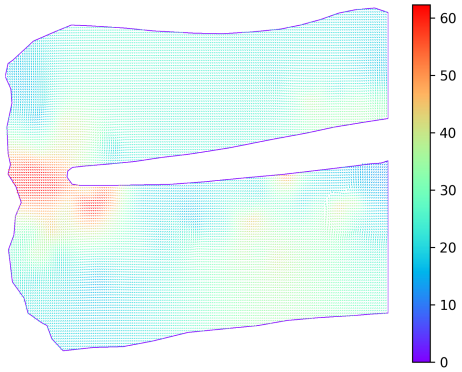

(c)

Fig. 8. Time dependent velocity vector field reconstruction. 8(a): result of reconstruction for the first hour. 8(b): result of reconstruction for the third hour. 8(c): result of reconstruction for the fifth hour.

we smoothed it considering the boundary value problem (2). The smoothing equation is composed of two terms, one that smooths the vector field and the other that keeps it close to the sparse-sample reconstruction. The parameter λ in the equation controls the ratio of influence of the two terms.

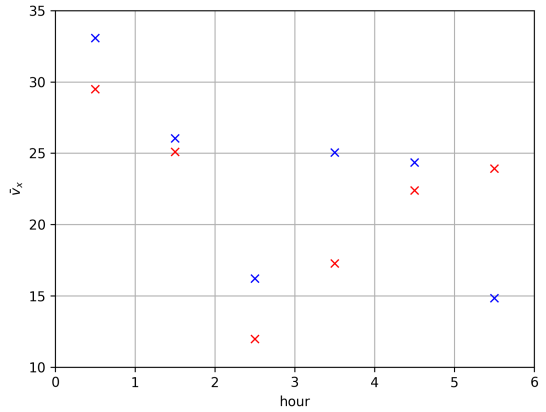

(a)

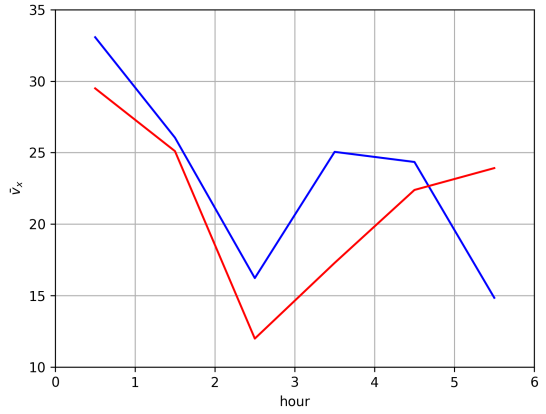

(b)

Fig. 9. Averaged velocity $\bar{v}_x$ in the direction to the wound for the 2 datasets during the time. 9(a): the results for the different datasets are depicted as crosses with different colors (blue and red) placed in the middle of the hour they represent. 9(b): the results for the different datasets are depicted as continuous lines with different colors (blue and red) with grid points placed in the middle of the hour they represent.

For all models considered, we proved the existence of a unique weak solution. For the discretization, we considered the finite difference scheme with unknowns placed on the vertices of a pixel grid. We then applied the vector field reconstruction to find the wound attractant field driving macrophages to the site of the wound during wound healing. In particular, we considered smoothing of the vector field and showed the influence of the parameter λ on the smoothing process. In addition, we reconstructed the wound attractant field in a time interval of 1 hour and showed the behavior of the average velocities in the direction of the wound for the different datasets. Reconstruction of the wound attractant field can bring insights into the behavior of the field over time, for example, about the rate of diffusion of the signal. Moreover, it will be possible to study the changes in the wound attractant field when the shape of the wound changes, in the presence of multiple wounds, or with subsequent wounds.

VI. Acknowledgment

We thank Resul Ozbilgic, Mai Nguyen Chi, and Georges Lutfalla from the University of Montpellier for providing the datasets for the analysis and their expert assistance.

This work has received funding from the European Union's Horizon 2020 research and innovation program under the Marie Skłodowska-Curie grant agreement No 955576 and by the grants APVV-23-0186 and VEGA 1/0249/24.

References

[1] F. Barros-Becker, P.Y. Lam, R. Fisher, and A. Huttenlocher. Live imaging reveals distinct modes of neutrophil and macrophage migration within interstitial tissues. *Journal of cell science*, 130(22):3801–3808, 2017.

[2] F. Ellett, L. Pase, J. Hayman, A. Andrianopoulos, and G. Lieschke. Mpeg1 promoter transgenes direct macrophage-lineage expression in zebrafish. *Blood*, 117(4):e49–e56, 2011.

[3] P. Friedl and B. Weigelin. Interstitial leukocyte migration and immune function. *Nature immunology*, 9(9):960–969, 2008.

[4] G. Gaël, J. Benoît and others. Eigen v3. http://eigen.tuxfamily.org, 2010.

[5] L. Li, B. Yan, Y.Q. Shi, W.Q. Zhang, and Z.L. Wen. Live imaging reveals differing roles of macrophages and neutrophils during zebrafish tail fin regeneration. *Journal of Biological Chemistry*, 287(30):25353–25360, 2012.

[6] G. Lupi, K. Mikula, and S.A. Park. Macrophages Trajectories Smoothing by Evolving Curves. *Tatra Mountains Mathematical Publications*, 86(1), 2023.

[7] G. Lupi, K. Mikula. Vector field reconstruction from sparse samples by triple-Laplacian. *Proceedings of the Conference Algoritmy*, 85-98, 2024.

[8] G. Lupi, S.A. Park, M. Ambroz, R. Ozbilgic, M. Nguyen Chi, G. Lutfalla, and K. Mikula. Mathematical and numerical methods for understanding immune cell motion. Submitted, available at arXiv: https://doi.org/10.48550/arXiv.2503.10552

[9] Z. Min. Electrical fields in wound healing— an overriding signal that directs cell migration. *Seminars in Cell and Developmental Biology*, 20(6):674–682, 2009.

[10] J. Nečas. Direct methods in the theory of elliptic equations. *Springer Monographs in Mathematics*, Springer, Heidelberg, 2012.

[11] S.A. Park, T. Sipka, Z. Krivá, M. Nguyen-Chi, G. Lutfalla, and K. Mikula. Segmentation-based tracking of macrophages in 2D+time microscopy movies inside a living animal. *Computers in Biology and Medicine*, 153:10649, 2023.

[12] K. Rektorys. Variational Methods in Mathematics, Science and Engineering. *Springer*, 2012.

[13] T. Sipka, R. Peroceschi, M. Groß, F. Ellett, C. Pescia, C. Gonzalez, G. Lutfalla, and M. Nguyen-Chi. Damage-induced calcium signaling and reactive oxygen species mediate macrophage activation in zebrafish. *Frontiers in Immunology*, 12, 2021.

[14] E. Van Goethem, R. Poincloux, F. Gauffre, I. Maridonneau-Parini, and V. Le Cabec. Matrix architecture dictates three-dimensional migration modes of human macrophages: differential involvement of proteases and podosome-like structures. *Journal of immunology*, 184(2):1049–1061, 2010.